Polar coronal holes during the past solar cycle: Ulysses observations

Rudolf von Steiger[1,2] and Thomas H. Zurbuchen[3]

Received 17 June 2010; revised 2 September 2010; accepted 18 October 2010; published 22 January 2011.

[1] During its nearly 19-year mission, Ulysses pioneered novel measurements of the three-dimensional heliosphere and particularly in situ observations of high-latitude solar wind from polar coronal holes (PCHs). Winds from PCHs exhibit constant elemental abundances to within the limits of the measurements, indicative of the fact that such winds truly provide a ground state of solar wind composition. However, these solar wind streams show long-term variability in the composition of ionic charge states frozen into the low corona. The C and O freeze-in temperatures measured in high-latitude solar wind have decreased ~10% as compared to the previous solar minimum and are now around 0.87 and 1.01 MK, respectively. The ionization states of Si and Fe also exhibit a substantial cooling with a reduction of 0.4 and 0.5 charge states, respectively. We show that these observations are indicative of an overall decrease of coronal temperature, forming a trend toward cooler PCH temperature persisting for over 14 years. We support these observations with a detailed and comprehensive description of the data analysis processes relevant for Ulysses SWICS and similar instruments.

Citation: von Steiger, R., and T. H. Zurbuchen (2011), Polar coronal holes during the past solar cycle: Ulysses observations, *J. Geophys. Res.*, *116*, A01105, doi:10.1029/2010JA015835.

1. Introduction

[2] On 30 June 2009, the Ulysses mission came to a close after 18 years and 8 months of uninterrupted and pioneering science measurements. During its heliospheric high-inclination orbit, Ulysses (a joint mission of ESA and NASA) has performed three entire polar passes, as indicated in Figure 1, and it has performed unparalleled scientific observations of the heliosphere. As part of its payload Ulysses carried the Solar Wind Ion Composition Spectrometer (SWICS) [*Gloeckler et al.*, 1992], which provided the first unambiguous measurements of solar wind heavy ions from He to Fe. The polar pass in 1994, marked S94 in Figure 1, led to the first detailed observations of solar wind originating from polar coronal holes (PCHs), which are the source of more than two thirds of the heliosphere near solar minimum [*von Steiger*, 1996]. Besides its high speed and unique dynamic signatures [*Bame et al.*, 1977], PCH-associated solar winds also exhibit compositional signatures in their heavy-ion components, which distinguish them from other, generally slower and more variable solar wind streams that are associated with streamers and tend to dominate the space environment near the ecliptic plane [*Geiss et al.*, 1995; *Zurbuchen*, 2007]. The ionization charge states of heavy elements indicate a substantially lower temperature of the solar wind source region, especially for C and O, whose ionization state is defined within the first 1.5 R_s above the photosphere [*Bürgi and Geiss*, 1986]; the elemental composition of heavy ions is nearly photospheric, in contrast to streamer-associated wind, which is enriched in elements with a first ionization potential (FIP) <10 eV [*von Steiger et al.*, 1997].

[3] Due to their rather constant and near-photospheric composition and dynamic state, the fast solar wind streams from PCHs have been referred to as the "ground state" of the solar wind, best suited for the analysis of the fundamental processes that shape its dynamics and compositional signatures. However, to the surprise of many, solar wind from PCHs observed on Ulysses has exhibited substantial changes during the time period from its pioneering measurements in 1994–1995 to the end of the Ulysses mission in 2009. During this time five periods of PCHs were observed, as indicated in Figure 1 and listed in Table 1. For this intercomparison, we define a PCH period to be confined to the region poleward of 70° heliographic latitude. We include in our analysis all high-latitude passes of the Ulysses orbit except the south pass in 2000–2001 during which (due to the near solar-maximum conditions) no PCH existed near Ulysses. Although still very much occurring near solar maximum conditions, the north polar pass in 2001 was dominated by fast solar wind and is therefore included in this analysis.

[4] It has already been reported that there are significant changes of the plasma properties of the solar wind between the polar passes in 1994–1995 and the 2007–2008 passes. Most importantly, the normalized radial magnetic field, a measure related to the polar cap field and the expansion rate

[1]International Space Science Institute, Bern, Switzerland.
[2]Physikalisches Institut, University of Bern, Bern, Switzerland.
[3]Department of Atmospheric, Oceanic and Space Sciences, University of Michigan, Ann Arbor, Michigan, USA.

0148-0227/11/2010JA015835

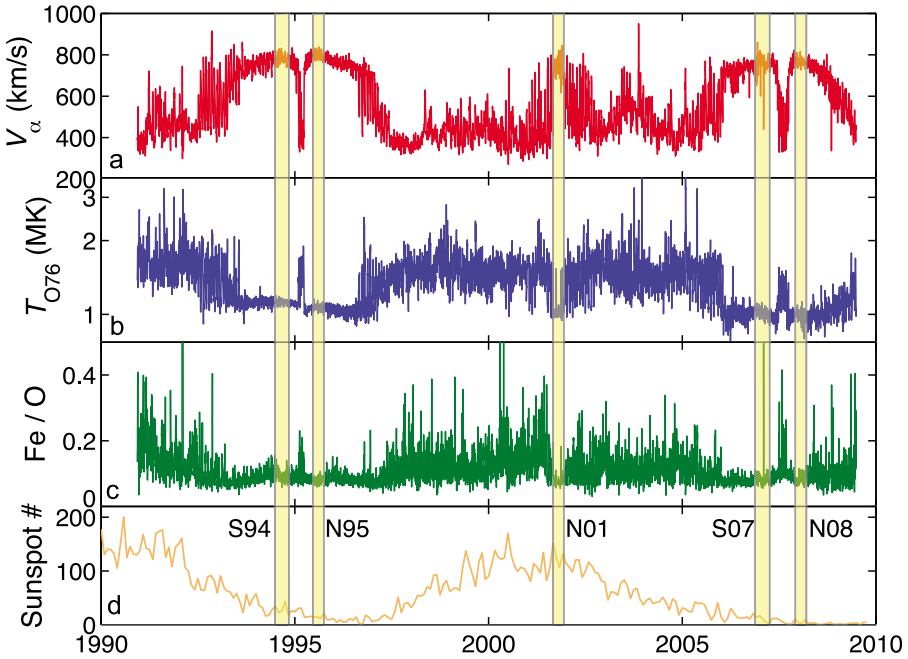

Figure 1. Overview of solar wind properties during the entire Ulysses mission: (a) solar wind speed, (b) freezing-in temperature derived from the O^{7+}/O^{6+} charge state ratio, (c) Fe/O abundance ratio, and (d) mean monthly sunspot number. The high-latitude passes when Ulysses was poleward of 70° heliolatitude are indicated by shaded bands, except for the south polar pass in 2000 as this was not dominated by a high-speed stream due to solar maximum conditions during that time period.

of the field in the low corona, changed by −14% [*Smith and Balogh*, 2008]. This is in contrast to a trend established during the past three solar minima, in which the radial field essentially returned to the same value [*Svalgaard and Cliver*, 2007]. During the same period, the solar wind flow was essentially weakened due a reduction in speed (−3%), density (−17%), and temperature (−14%), resulting in a reduction of mass flux by 20% and of dynamic pressure by 22% in the solar wind from PCHs [*McComas et al.*, 2008].

[5] The analysis of heavy ions during this time period is crucial due to their diagnostic power of the solar source region through detailed measurements of their elemental composition and freeze-in processes. This paper investigates compositional changes during this time period. In section 2 we will investigate whether the PCH elemental composition shows significant changes during this time period. Section 3 will be focused on the analysis of substantial and systematic changes in the PCH freezing-in temperatures, and in section 4 we will interpret and discuss these results. Appendix A provides a comprehensive analysis of the methodology used for this paper with focus on an accurate description of absolute and relative errors of the results.

2. Elemental Abundances of C, O, Si, and Fe

[6] The elemental abundances of solar wind from PCHs for the passages of S94 and N95 (see Figure 1) have been analyzed previously by *von Steiger et al.* [2000]. This analysis focused on all heavy elements detected with SWICS. It was based on daily averages of SWICS data and analyzed both the average and standard deviations of each of the contributions. There were two key conclusions from this analysis. First, the two polar passes exhibited elemental compositions identical to within the measurement accuracy of typically 20% provided by SWICS. Second, the elemental abundances observed in the heliosphere exhibited measurable deviations from the photospheric composition. These deviations were most pronounced in He/O where the solar wind He is reduced by over 35%, and also with a small fractionation effect affecting all elements according to their first ionization potential (FIP), that is, elements with increasing FIP are suppressed relative to their photospheric composition. This fractionation process is much enhanced in streamer-associated slow wind (references in *von Steiger et al.* [2000] and *Zurbuchen* [2007]). Furthermore, the variability of any given compositional quantity is also increased in slow wind relative to wind associated with PCHs. Figure 2 summarizes the

Table 1. High Latitude Passes of Ulysses at Poleward of 70° Heliolatitude[a]

Period	Start Date	End Date (Included)	Duration (Days)
S94	177-1994	309-1994	132
N95	170-1995	272-1995	103
(S00	250-2000	016-2001	133)
N01	242-2001	344-2001	90
S07	323-2006	094-2007	138
N08	335-2007	074-2008	105

[a]Period S00 was not included in the further analysis because it was not dominated by a coronal hole-associated fast stream. The duration of period N01 is shorter than the simple time difference because of the omission of certain days from the analysis due to the occurrence of CMEs; see text.

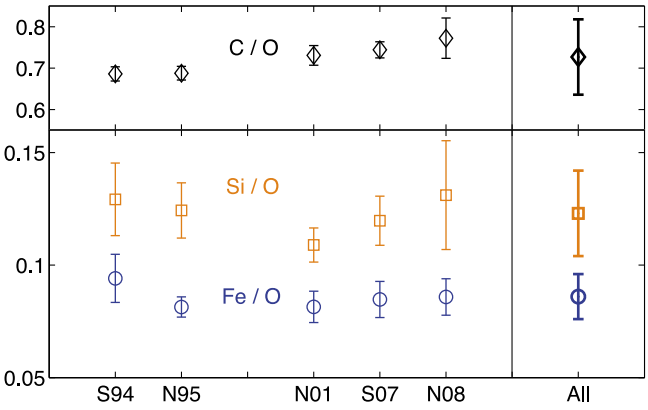

Figure 2. Element abundance ratios of carbon, silicon, and iron relative to oxygen observed in polar coronal holes. Each data point represents the average of all 10 day values obtained during the respective period and the error bars indicate their standard deviation. The thick values on the right denote the mean of all periods with the systematic error as given in equations (1)–(3) and discussed in the Appendix A.

average C/O, Si/O, and Fe/O elemental abundance ratios together with their standard deviation for each of the five polar passages from Table 1 using the very same methods previously discussed in *von Steiger et al.* [2000].

[7] Here, we use 10-day averages of each elemental composition ratio, averaged for all periods that Ulysses spent at a heliospheric latitude >70°. The use of 10 day averages as opposed to daily averages used in *von Steiger et al.* [2000] is due to a trade-off between statistical accuracy and inversion methodology, as described in detail in Appendix A. Three specific time periods in the 2001 polar pass were excluded from the analysis because each was previously shown to be associated with the eruption of a coronal mass ejection (CME), temporarily immersing Ulysses in CME-associated plasma and not PCH plasma. For a description of these events, refer to *von Steiger et al.* [2004]. They can also be identified as short-time enhancements of the oxygen freezing-in temperature, which is typical for a majority of CMEs [*Zurbuchen and Richardson*, 2006], as seen in Figure 1.

[8] The statistical error of each daily time period is approximately a few percent (see Appendix A for a discussion of all statistical and systematic errors). The Ulysses data coverage during these time periods is well over 90%, with the exception of period N08, when it drops to ~70% after 15 January 2008, due to the loss of X-band communications.

[9] Figure 2 demonstrates that the elemental composition remains constant to within the SWICS measurement uncertainty. The small (<10%) increasing trend in the C/O ratio is considered spurious since it is of the order of the systematic uncertainty of the detector efficiencies (see Appendix A). For Si and Fe the averages are similar with their error bars overlapping for each of the time periods in question. We have performed a t test with the usual 5% significance level to confirm that the five samples of Fe/O and of Si/O are drawn from a single normal distribution for each element, with the exception of Si/O in period N01 that just escapes a positive test result. The mean abundance ratios with their purely statistical standard deviations and their systematic uncertainties as detailed in Appendix A are

$$\mathrm{C/O} = 0.727 \pm 0.006(\mathrm{stat}) \pm 0.091(\mathrm{syst}), \quad (1)$$

$$\mathrm{Si/O} = 0.123 \pm 0.002(\mathrm{stat}) \pm 0.019(\mathrm{syst}), \quad (2)$$

$$\mathrm{Fe/O} = 0.086 \pm 0.001(\mathrm{stat}) \pm 0.010(\mathrm{syst}). \quad (3)$$

These values are shown on the right-hand side of Figure 2.

[10] Thus, the elemental abundances provided in *von Steiger et al.* [2000] therefore provide a valid measurement for each of the PCH periods. Furthermore, Figure 2 provides credence to the notion that PCH-associated wind indeed is a ground state of the solar wind, while it is further fractionated in CME and in streamer plasma. The analysis of variations on smaller timescales are limited by statistical and systematic errors and should not be over-interpreted [*Gloeckler and Geiss*, 2007]. On the contrary, the physical processes governing FIP fractionation in the chromospheres do not appear to be substantially affected by the changing dynamic properties already discussed and by the coronal temperature changes analyzed below.

3. Charge Composition of C, O, Si, and Fe

[11] The distribution of ionic charge states of a given element is determined by collisions with hot electrons in the inner corona where most of the energy deposition and heating of the open corona occurs [*Hundhausen et al.*, 1968; *Bürgi and Geiss*, 1986]. Upon expansion into the solar wind these ionic charge states are first in equilibrium with the electrons, but then freeze in individually when their total collision timescale with the electrons approximately equals the expansion timescale of the wind. Since the recombination timescale increases with distance from the Sun due to the decreasing electron density (assumed to decrease monotonously), those charge states with the shortest recombination times freeze in closest to the Sun. The charge states of different elements can thus be used to deduce a rough temperature profile of the corona [*Geiss et al.*, 1995].

[12] In order to compare freeze-in distributions of elements with substantially different numbers of ionic charge states and also different freeze-in locations, we express the average charge state of each element in units of temperature, as follows:

[13] For Si and Fe we first determine the average charge state $\langle q \rangle$ from a weighted average of the measured charge state densities, n_q,

$$\langle q \rangle = \frac{\sum q n_q}{\sum n_q}. \quad (4)$$

We then calculate the temperature, T_q, whose ionization balance calculated according to *Mazzotta et al.* [1998], best fits the measured average charge state. This transformation from $\langle q \rangle$ to T_q ($\langle q \rangle$) is unique.

[14] For O and C, we used a limited set of charge distributions to calculate a freeze-in temperature, for consistency

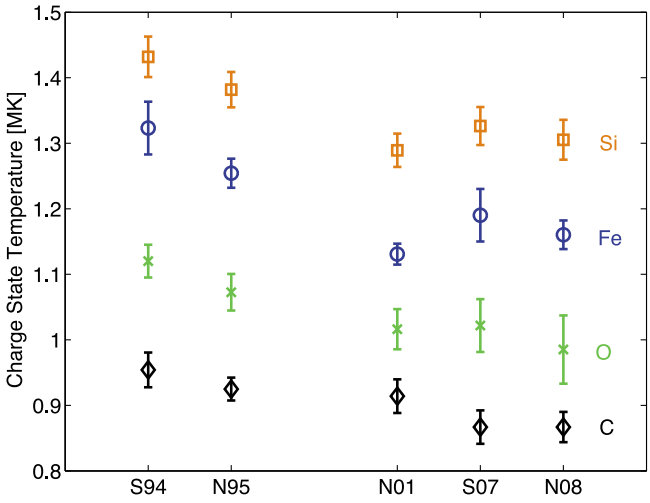

Figure 3. Coronal hole-associated charge state temperatures of silicon, iron, oxygen, and carbon. Each data point represents the average of all 10 day values obtained during the respective period and the error bars indicate their standard deviation.

following the method previously used according to $T_O = T_q$ (O^{7+}/O^{6+}) and $T_C = T_q$ (C^{6+}/C^{5+}) [*von Steiger et al.*, 1997]. A freeze-in temperature calculated from the full charge state distributions agrees to within a few percent of the one computed with this reduced approach.

[15] Figure 3 provides the charge state temperature values from C, O, Si, and Fe for all periods analyzed here. Again, we used 10-day averages during high-latitude passes described in the previous section, and we excluded the CME time periods in 2001 as previously discussed as well. Error bars are indicative of statistical and systematic errors but are approximately equal to the standard deviation of the distribution of 10-day averages. Thus, the overall sizes of the error bars mostly reflect the statistical accuracy of the estimate.

[16] There is an obvious and significant decrease of the charge state temperature for every element by approximately 10%. The average Si and Fe charge states decrease by 0.15 and 0.2, respectively, from S94 to N08. This decrease is clearly significant because it is larger than the average scatter of each of the data points of a given time period and because it is shared between all considered elements. Moreover, ratios of charge states of the same element are less affected by the systematic uncertainty in the detector efficiencies as compared to element ratios, as discussed in Appendix A.

[17] The temperature decrease is further illustrated in Figure 4, which shows the distribution of all 10-day averages of T_O and T_C pairs for the five PCH periods discussed here. Two-dimensional error bars are provided to demonstrate that the decrease between periods SS95-N95 and S07-N08 is significant and not due to a statistical fluctuation, as it substantially exceeds the size of the error bars. Figure 4 also includes a line of equal temperatures (i.e., $T_O = T_C$), which shows that the freezing-in of C and O does not occur at the same location. Both, C and O charge states are known to freeze in very close to the Sun [*Bürgi and Geiss*, 1986; *Geiss et al.*, 1995], but C has a shorter recombination time, causing freeze-in to occur at a higher density and therefore closer to the Sun as compared to O. This ordering remains the same for each of the time periods as both T_O and T_C move to progressively smaller values. The temperature decrease follows pretty much the same trend, $T_O = 1.18T_C$, that has been found to apply for all solar wind types [*von Steiger*, 2008].

4. Interpretation and Discussion

[18] This comparative technique provided in Figure 4 can be used for all measurements in Figure 3. Considering the size ordering of the recombination rates of the different elements the vertical order of the freeze-in process may be inferred. Figure 5a sketches a radial ordering and approximate freeze-in range based on the measured C, O, Si, and Fe charge state temperatures in 1994 (S94 in Figure 1) and on estimates of the freezing-in altitudes by *Bürgi and Geiss* [1986], assuming a monotonically decreasing density profile with distance. This is identical to the sketch provided by *Geiss et al.* [1995].

[19] There are two different physical scenarios that could be responsible for the observed cooling of the charge state temperatures from 1994 to 2008. First, the observed changes could be caused by changes of the freeze-in location with an unchanged electron temperature profile, such as caused by a decreased density profile or an increase of velocity. Based on the in situ plasma observations a systematically decreased density is most likely, as sketched in Figure 5a. Second, the observed changes could be indicative of a cooling of the coronal temperature, as indicated in dashed lines in Figure 5b. We will now argue that only this second scenario is consistent with our observations.

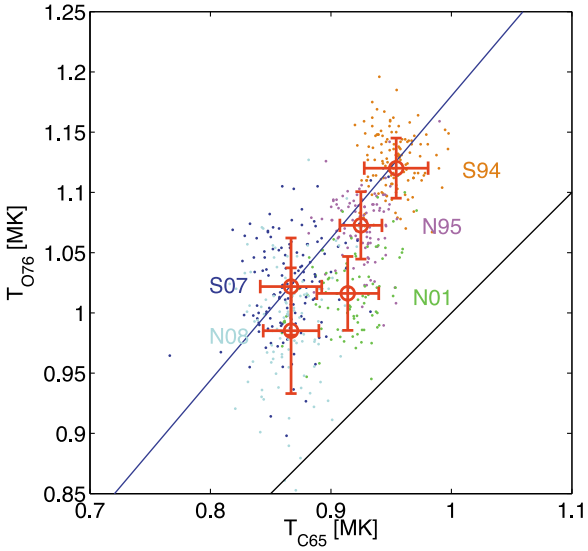

Figure 4. Charge state temperature distribution of T_O vs. T_C. Each data point represents an individual 10 day spectrum, and their averages for each high-latitude pass are indicated with error bars. The black line indicates equal temperatures ($T_O = T_C$), and the blue line represents the best correlation of the data, $T_O = 1.18T_C$.

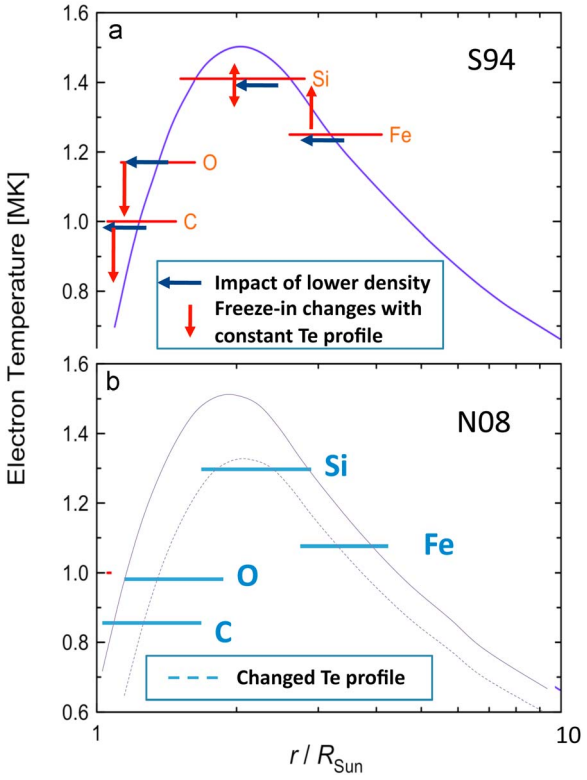

Figure 5. Coronal temperature profile in the periods (a) S94 and (b) N08. The observational result that all charge state temperatures are lower in N08 as compared to S94 cannot be explained by a shift of the freezing in locations due to a lower density profile but only by an overall cooling of the polar corona between 1994 and 2008.

[20] Consider first a hypothesis that the reduced overall changes are caused by a reduction of the solar wind density (as observed by *McComas et al.* [2008]), but with an approximately unchanged temperature profile, as shown in Figure 5a. The reduction of the density causes the freezing-in to occur systematically earlier in time, moving the location where freeze-in is occurring closer toward the Sun. This is indicated with blue horizontal arrows. Assuming that the electron temperature remains the same, this shift in freeze-in radius would then result in a change of freeze-in temperature reflecting the temperature gradient at each location, indicated by vertical red arrows. For C and O, this change is predicted to lead to a decrease of their charge state temperatures, as is observed (cf. Figure 3). For Si, this change can result in either a positive or a negative temperature change, depending on the exact location of the Si freeze-in relative to the location of the temperature maximum in the corona, again possibly consistent with our observations in Figure 3.

[21] However, Fe freezes in at such high altitudes in the corona where the coronal electron temperature is decreasing with heliocentric distance, owing to its high ionization and recombination coefficients [*Geiss et al.*, 1995]. Consequently, for Fe the observed shift of the freeze-in location would predict a net increase of the Fe charge state temperature. This is inconsistent with our observations of Fe charge state temperatures, which appear to be correlated with the C and O temperatures in all cases.

[22] We therefore reject this first scenario: The observed changes in charge state temperatures cannot be solely caused by changes in the freeze-in locations due to a density decrease. Instead, our results suggest a significant change of the coronal temperature profile and heating processes for these observed PCH periods. This is sketched in Figure 5b. Horizontal bars indicate the charge state temperatures provided in Figure 3 for the N08 time period, at a radius range approximately consistent with freeze-in calculations by *Bürgi and Geiss* [1986]. The dashed line sketches a notional temperature profile consistent with our observations. For comparison, the S94 curve is shown as well.

[23] This derived temperature profile is substantially different from earlier estimates in all parts of the outer corona analyzed here. In particular, this change is expected to have important consequences for the UV/EUV emission characteristics of the corona, which is known to be strongly temperature dependent [*Wilhelm et al.*, 1998]. We do not know whether a dimming of the optical emission from the polar coronal holes by the expected factor of $0.9^4 \simeq 0.66$ has been observed during the current solar minimum as compared to the previous one.

[24] Together with additional observational and theoretical constraints, our data provide a unique opportunity for unprecedented tests of the physical models that lead to coronal heating. For instance, *Laming and Lepri* [2007] suggest that the electron heating might occur through lower hybrid waves excited by density gradients in the solar wind flow and the perpendicular heating of ion cyclotron waves. If this is indeed the dominant mechanism for electron heating in the outer corona, our observations indicate that this mechanism is inhibited in PCH during 2008 as compared to 1994. This could be caused by a reduction of free energy from the chromosphere, possibly leading to observable constraints of this process.

[25] We also note a significant difference of the relative freeze-in temperature changes in N01 as compared to all other PCHs. This time period exhibits the lowest Si and Fe charge states of all periods under consideration, although the C and O data fall in line nicely with a general decrease of the charge state temperature during the entire period. As compared to C and O, Si and Fe freeze in at larger solar distances, as shown in Figure 5b and are therefore sensitive to large-scale expansion properties that differ near solar maximum (N01) as compared to the solar minimum-type situations.

5. Summary

[26] Solar wind from polar coronal holes has long been considered to be the basic, fundamental type of solar wind emitted into the heliosphere. During a solar cycle it contributes about 50% of all solar wind and even more during solar minimum. The constancy of the elemental abundance of this wind during five extended periods of observations gives credence to this notion. However, there are important changes in the ionic charge states of that wind and, related to that, also in the dynamic properties of this wind. We have shown that these changes are due to a significant reduction of the overall electron temperature in the entire corona by about 10%.

[27] Interestingly, this PCH reduction in temperature is steady from 1994 to 2008 in almost all charge state indicators when we disregard the intervening maximum period (N01). We do not currently know whether this trend will be reverted after the recovery of the Sun-heliosphere system from the current solar minimum. During the maximum period N01 all temperatures are closer to each other indicating a slightly modified thermal profile in the corresponding maximum coronal hole as compared to the minimum holes.

[28] Our interpretation of the freeze-in temperatures generally assumed thermal electron distributions. This is well-supported by previous modeling results [*Ko et al.*, 1996], but there are models that emphasize the importance of non-thermal effects for electron distribution functions in the corona [*Owocki and Scudder*, 1983; *Laming and Lepri*, 2007].

[29] We also note that the accompanying reductions in the heliospheric magnetic field, solar wind density, and temperature in wind from PCHs provide unique opportunities to test models for the heating and acceleration of the corona and solar wind. We expect that the presented freeze-in temperatures and their variations will become an important part of such studies.

Appendix A: Accuracy of SWICS Data

[30] The overall methodology used for the analysis of SWICS data has been described in detail by *von Steiger et al.* [2000] and particularly in Appendix A of that paper. The analysis methodology described there has been used routinely during a decade of data analysis of composition data from Ulysses, ACE, and other composition instruments.

[31] Here, we focus on the analysis and derivation of the uncertainty of the data inversion rather than the overall process described by *von Steiger et al.* [2000]. The sound justification of these uncertainties is critical for the interpretation of the results provided in this paper and also in other publications (future or past) using SWICS data with an analysis methodology comparable to the one described by *von Steiger et al.* [2000].

[32] This methodology is designed to convert a series of individually measured particles into distribution functions of individual ion species as shown in Figure A1 that shows part of a long-term analysis over a representative 10 day period. Figure A1a first provides energy distributions of count rates as a function of E/q of selected ions. A single E/q level E/q = 10.015 keV/e is marked on this chart, for which all individual measurements in energy time-of-flight space are indicated in Figure A1b. There, individual ion species are marked in the form of ellipses defined according to the forward model used in this analysis.

[33] The challenge of the SWICS data analysis is twofold. First, individual ion measurements as shown in Figure A1b have to be associated with specific ions. Second, the analysis methodology has to allow for an inversion of measured count rate of a given ion measured as a function of E/q, $C_i(E/q)$, into the differential flux

$$dj_i(E/q) = \frac{C_i(E/q)}{t_{\mathrm{acc}} g \eta_i(E/q, \alpha)}. \quad \text{(A1)}$$

Here t_{acc} is the accumulation time, g is the geometric factor, and $\eta_i(E/q,\alpha)$ is the detector efficiency that is dependent on the type of the ion species, i, the energy per charge ratio of the incident ion, and also the so-called aspect angle α, which is the angle between the spacecraft rotation axis and the solar wind direction (see *von Steiger et al.* [2000]). The derived $dj(E/q)$ values can then be transformed into observed values of the distribution function which form the basis of all results derived from SWICS.

[34] There are a number of sources of uncertainties and errors that affect both steps of this inversion of SWICS measurements and which are now discussed in detail. Our discussion will follow the summary of errors and uncertainties provided in Table A1.

A1. Limited Count Rate of Ions

[35] The statistical accuracy, $s_C^2 = (\Delta C_i/C_i)^2$, of any given measurement directly relates to the total count rate according to Poisson statistics (i.e., $s_C = 1/\sqrt{C_i}$). The count rate is strongly dependent on abundance, density, and heliocentric distance. For a typical 10 day interval, the statistical accuracy of a given ion species measurement is shown in Figure A2. The actual time period used in Figure A2 is the 10 day period starting on 25 June 1995 but is representative for all time periods analyzed for this paper. Typically the statistical uncertainty is a few percent for individual charge states; it exceeds 10% only for the rarest ones. Since elemental abundances are simply obtained from summing over all charge states their statistical uncertainties are at least as good as that of the dominant charge state. For He, C, and O this is <1% and for the other elements it is <3%.

A2. Misidentification of Ions Due to Inaccurate Self-adjusting Forward Model

[36] The forward model locations in energy and time of flight shown in Figure A1b are optimized during the inversion process as detailed in *von Steiger et al.* [2000]. To check the impact of systematic errors from such adjustments (especially in the limit of low counting statistics) a series of data inversions were performed during all polar passes defined by Table 1. During these experiments, a number of temporal resolutions were used varying from 1 day to 100 days and the autonomously optimized locations of all ion species were compared.

[37] Based on this analysis we conclude that the self-adjusting forward model is highly robust and leads to changes of <0.1 time-of-flight channel and <1 energy channel, leading to an estimated systematic error of less than 0.5%.

A3. Misidentification of Ions Due to Substantially Overlapping Peaks

[38] This error source is caused by the finite resolution of SWICS in both time-of-flight and total energy, as shown in Figure A1b (see also section 2.3.1 in *von Steiger et al.* [2000]). The probability of a given count being associated with a certain ion species depends not only on its vicinity to the anticipated location in the SWICS forward model but also on the location and height of neighboring peaks. The ability to resolve two neighboring peaks further depends on the total number of counts available.

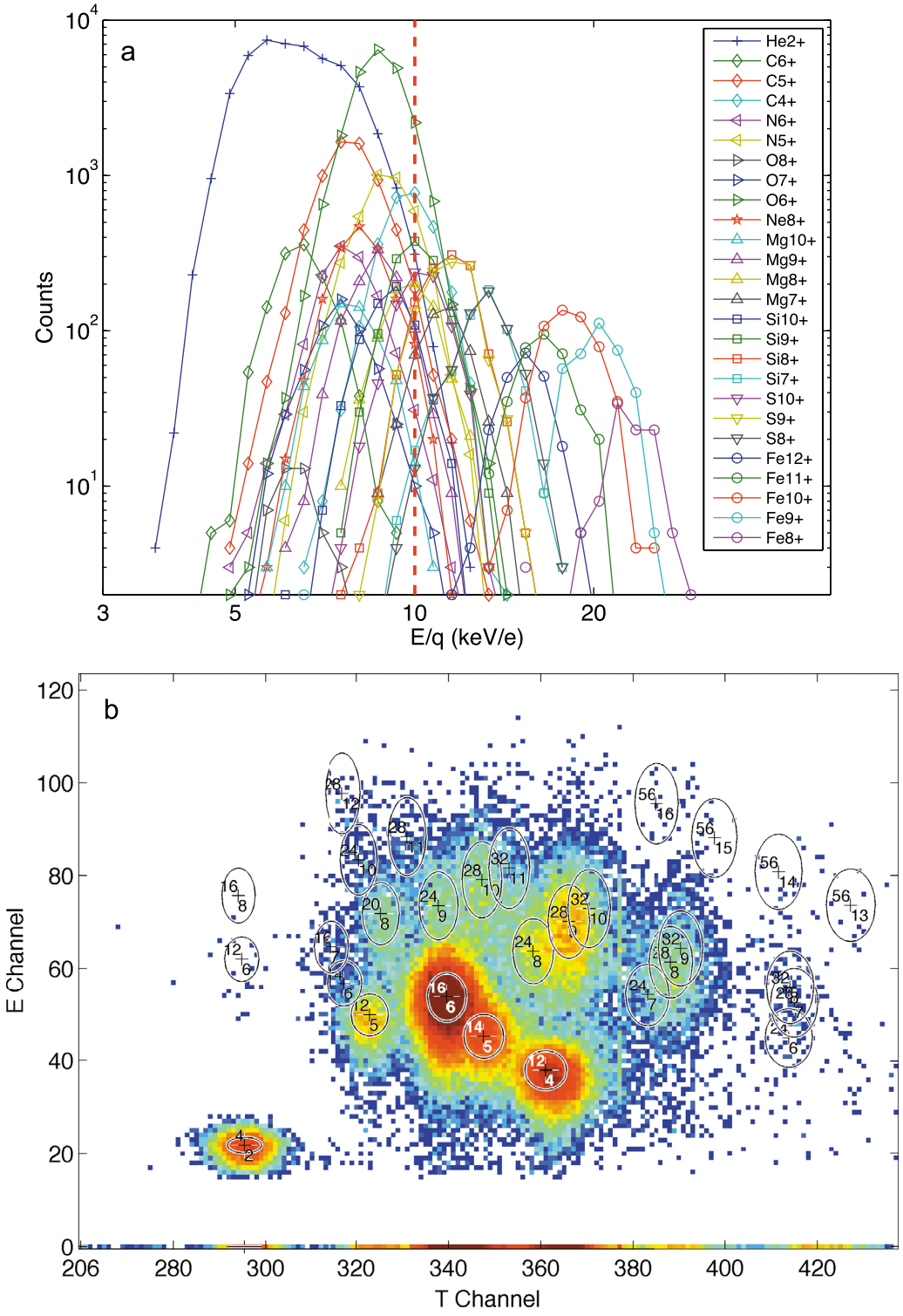

Figure A1. (a) Energy-per-charge count-rate spectra of different ion species during a representative 10 day period observed with Ulysses-SWICS. (b) Time of flight vs. total energy matrix observed with Ulysses-SWICS at one particular energy-per-charge setting (E/q = 10.015 keV/e).

[39] Consider, for example, the ability to resolve two specific neighboring ion species in Figure A1b. The abundant O^{6+} will affect the ability to resolve N^{5+}, which is much less abundant. Yet, successful separation can be achieved as long as N^{5+} includes enough measured counts for a Gaussian inversion to be successful. On the other hand, consider the ability to separate S^{8+}, Si^{7+}, and Mg^{6+}. Successful separation is hampered for two reasons: the peaks overlap in this and many other E/q slices, and their abundance is small.

Table A1. Sources of Statistical and Systematic Errors and Their Impact on the Accuracy of Solar Wind Abundances from SWICS

Source of Uncertainty	Quantity Affected	Type of Error	Effect on Absolute Fluxes	Effect on Relative Abund.
Limited count rate of ions	$C_i(E/q)$	Statistical	Variable (Figure A2)	Variable (Figure A2)
Misidentification of ion due to inaccurate self-adjusting forward model	$C_i(E/q)$	Systematic	0.5%	0.5%
Misidentification of ion due to substantially overlapping peaks	$C_i(E/q)$	Systematic, strongly dependent on statistics	Variable (section A3)	Variable (section A3)
Uncertainty in absolute geometric sensitivity	g	Systematic	10%	0%
Error in accumulation time	t_{acc}	Systematic	1%	0%
Detector efficiency errors	$\eta_i(E/q,\alpha)$	Systematic	10% for He, C, O, Ne; 15% for others	10% for element ratios, 5% for charge state ratios
Temporal evolution of efficiency	$\eta_i(E/q,\alpha)$	Systematic	2%	2%
Observational changes during integration time	$\eta_i(E/q,\alpha)$	Systematic	8% for t_{acc} >10 day, <3% for shorter periods	0%

[40] Our inversion code is very successful with the former situation, as long as there are sufficient statistics. Yet, in the latter situation, counts are more difficult to be attributed to a certain ion species. Our probabilistic scheme (described in *von Steiger et al.* [2000]) for count identification assigns an identity to each count based on its proximity to the elliptical regions and to the number of counts contained in each one of them. If the latter is down to very few scattered counts the chances for misattributions become appreciable.

[41] These inversion errors have been investigated in a series of experiments in which the duration of the accumulation of individual spectra was varied (1 day, 10 days, and the entire high-latitude passes of ~100 days). Taking advantage of the constancy of coronal hole abundances, we have experimentally verified that the abundances of all well-resolved ion species such as iron are independent of the time resolution and remain stable (see Figure A3). For shorter accumulation periods (1 day), statistical limitations may lead to the elimination of least abundant charge states. However, the elemental abundances are little affected as they are dominated by the abundant charge states and thus remain reliable at all time resolution. On the other hand, the abundances of overlapping peaks are more difficult to assess and misidentifications occur in particular at low statistics or high time resolution. This is also illustrated in Figure A3 with the abundances of silicon and sulfur. At the highest resolution (1 day) many Si counts obviously get misattributed to Mg (and also to S), which is thus biased to a higher abundance at the cost of Si. Only at 10 day resolution the statistics become good enough to separate these elements more reliably. This is why we have used 10 day abundance measurements in the main body of this paper. Note, however, that the effect can be minimized, if not altogether eliminated, by using only the sum of the relevant abundances, as has been done by *von Steiger et al.* [2000] in their definition of the FIP fractionation factor, f (their equation (4)).

[42] The problem of overlapping peaks discussed above can also be addressed with a different technique, as follows. To reliably diagnose this problem, we use derived velocity distribution functions as shown in Figure A1a. It is well known that heavy ions in the solar wind have approximately the same bulk speed and the same thermal speed (i.e., approximately a mass-proportional temperature). That is particularly true at large heliocentric distances where the heliospheric magnetic field is likely to be perpendicular to the radial direction and, due to the negligible cross-field transport of thermal particles, all heavies are expected to have the same radial speed as measured by SWICS [*Hefti et al.*, 1998; *von Steiger and Zurbuchen*, 2006]. Misidentifications are reliably identified as significant deviations from these scaling

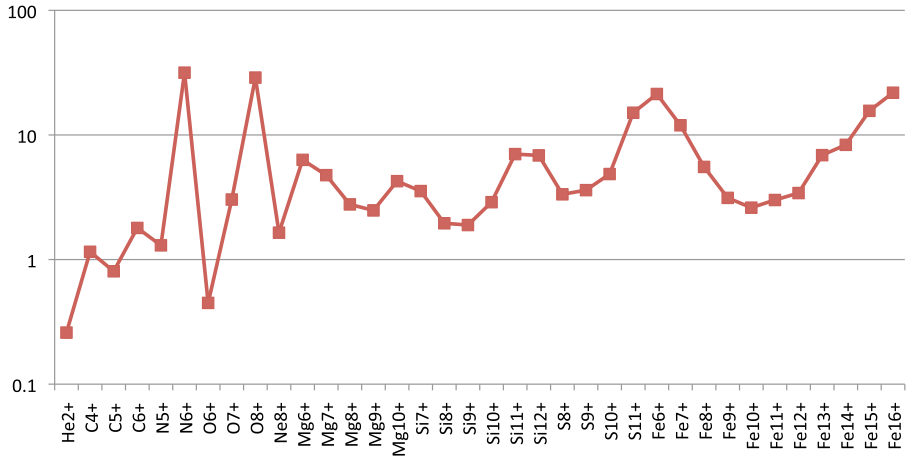

Figure A2. Percentage statistical accuracy of different ion species identified with SWICS during a typical 10 day period during a high-latitude polar pass. The statistical accuracy varies over nearly a factor of 100 but is in the <20% range for all ion species of relevance for this study.

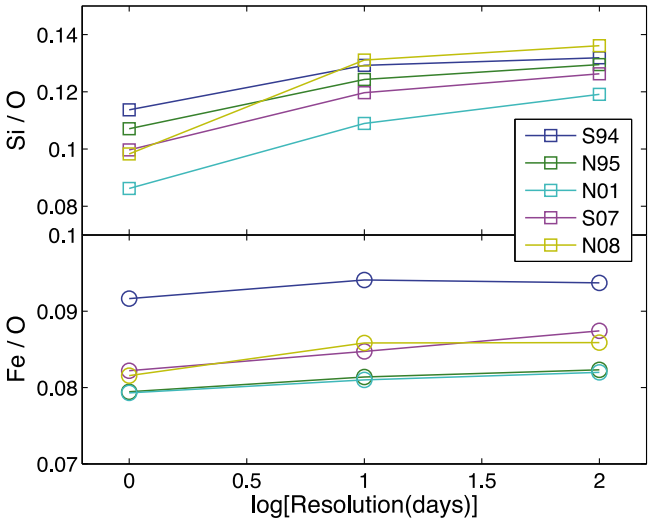

Figure A3. Abundances of Si and Fe relative to O measured during the five high-latitude periods (according to Table 1) of Ulysses as a function of the time resolution used in the analysis. While Fe/O is largely independent of the resolution owing to its well-separated ions in the E-T matrices, Si ions tend to get confused at high (1 day) time resolution. At integration periods exceeding 10 days, the abundances remain stable.

laws, and through apparent and nonphysical abrupt jumps in velocity distributions, caused by E/q -dependent misattributions of ion species.

[43] The effect is difficult to assess quantitatively because it is different for each individual charge state depending on its neighbors in the measured E-T matrix (see Figure A1b). For 10 day spectra it is virtually zero for He and very small for Fe (~2%), somewhat larger for C and O (≤5%), even larger for Ne, Mg, and Si (≤10%), and quite large for N and S (~20%). Because each charge state is affected individually the error is basically the same for absolute and for relative abundances.

A4. Uncertainty in Determination of Absolute Geometric Sensitivity

[44] The geometric factor, g, measures the absolute geometric sensitivity of the instrument and has been derived through extensive laboratory measurements and also in flight tests. We consider the accuracy of this measurement on absolute flux measurements to be 10%. Yet, this uncertainty does not affect abundance ratios.

A5. Error in Accumulation Time

[45] Similarly, the accumulation time, t_{acc}, can be slightly wrong due to timing uncertainties within the instrument's data processing unit, settling time of voltages in the high-voltage analyzers, and the capacitance of the SWICS electrostatic analyzer system which effectively changes the accumulation time. Based on laboratory tests prior to flight, we consider this uncertainty to be <1%. This uncertainty again does not affect abundance ratios.

A6. Detector Efficiency Errors

[46] Detector efficiency errors provide some of the most important limitations of SWICS (section 2.3.2 of *von Steiger et al.* [2000]). When Ulysses-SWICS was calibrated, sources for solar wind-like high charge state ion species were not routinely available, and only singly charged and doubly charged ion beams were used for calibration. The detector efficiencies are then extrapolated using a model to cover all elements measured with SWICS and the entire energy and time-of-flight range SWICS operates in *von Steiger* [1995]. Subsequent calibrations with the sister instrument of Ulysses SWICS on ACE [*Gloeckler et al.*, 1998] have provided measurements in a more extensive range and the efficiency model has found to be very much reliable.

[47] Some uncertainty remains because the instrument is used in an energy range and for elements for which it could not be calibrated. However, the typical detector efficiencies for most ion species are quite large, >30% for all relevant species and even >50% for most of them, all lying on curves that asymptotically approach 100% at higher energies. The relative uncertainty of such a sizable efficiency is of course much better than if it were only a few percent. We have conservatively estimated the uncertainty of the detector efficiency for absolute abundances at about 10% for those elements that were available in the calibration facility (He, C, O, and Ne) and at about 15% for other elements.

[48] This uncertainty applies also to element abundance ratios since different elements are characterized by different, individually calibrated efficiency curves. However, the situation is much better for ratios of different charge states of the same element. Since their efficiencies lie on the same curve it basically cancels when taking the ratio, and there remains only a small uncertainty related to the derivative of the efficiency. We therefore think that charge state ratios and the freezing-in temperatures derived therefrom are accurate to 5% or better.

A7. Temporal Evolution

[49] The sensitivities of particle detectors have a tendency to change over time. For the SWICS instrument, the most important changes are expected to occur due to the well-known efficiency changes from multichannel plates (MCP), which are used for the detection of start and stop signals that are then assembled to a valid time-of-flight measurement for each of the detected ions [*McFadden et al.*, 2007]. We have analyzed the MCP efficiencies during the entire period of operation of nearly 19 years and have found that the expected efficiency decreases are small compared to the efficiency errors typically used in the previous section.

[50] During their life-time operation, the curved-channel MCPs used in SWICS have detected ~5×10^{10} events. This was determined using a detailed life-time integral of all counts (background and ion signals) for SWICS. Each of these start pulses created a statistical average of 1.1 electrons [*von Steiger*, 1995]. Using a calibrated MCP gain of 2×10^6 electrons per incident electron, we can calculate the total charge that was extracted from the SWICS MCPs over an estimated area of ~2 cm^2. We obtain a life-integrated charge of <0.01 C/cm^2 for the SWICS MCPs, which is well below the specification for the plates used [*Timothy*, 1981].

[51] We have also analyzed the long-time evolution of the SWICS efficiency by comparing time series of measured sensitivities for a given energy, mass, and charge of an incident ion. Typically, we performed our analysis for He^{2+} due to the statistical significance of this measurement during one instrument cycle and because of the fact that these measurements only have very small background. A detailed analysis over the entire SWICS energy range has revealed that efficiency changes are small (i.e., <0.3%/yr) which is much smaller than the uncertainty of the laboratory measurements and model calculations used to determine SWICS efficiencies (section A6).

A8. Systematic Observational Changes Within Integration Time

[52] During its heliospheric orbit, the orientation of the Ulysses spacecraft was systematically changed to enable telemetry downlinks using a hard-mounted spacecraft radio system. This systematic orientation change affects the efficiency, $\eta_i(E/q,\alpha)$, through the change of the so-called Sun aspect angle, α, and therefore the effective duty cycle of the instrument. From our inversion experiments using various durations of accumulation described above, we also concluded that we had to limit the maximum accumulation time to a time period substantially smaller than the time period during which such changes are taking place. For this analysis, limiting ourselves to 10 day accumulations, allows that changes are within 3° and therefore not essentially affecting the duty cycle (see section A 3.1 in *von Steiger et al.* [2000]), except for brief periods when the aspect angle is very small, $\alpha < 5°$.

[53] **Acknowledgments.** This work is supported, in part, by JPL contract 1268016 and NASA grant NNX09AH72G. T.H.Z. acknowledges the hospitality of the International Space Science Institute where most of this work was performed. We acknowledge the many individuals who, during more than 30 years, have contributed a truly unique data set from Ulysses and particularly the SWICS instrument.

[54] Philippa Browning thanks Eberhard Moebius and another reviewer for their assistance in evaluating this paper.

References

Bame, S. J., J. R. Asbridge, W. C. Feldman, and J. T. Gosling (1977), Evidence for a structure-free state at high solar wind speeds, *J. Geophys. Res.*, *82*, 1487–1492.

Bürgi, A., and J. Geiss (1986), Helium and minor ions in the corona and solar wind: Dynamics and charge states, *Sol. Phys.*, *103*, 347–383.

Geiss, J., et al. (1995), The southern high-speed stream: Results from the SWICS instrument on Ulysses, *Science*, *268*, 1033.

Gloeckler, G., and J. Geiss (2007), The composition of the solar wind in polar coronal holes, *Space Sci. Rev.*, *130*, 139.

Gloeckler, G., et al. (1992), The solar wind ion composition spectrometer, *Astron. Astrophys. Suppl.*, *92*, 267–289.

Gloeckler, G., et al. (1998), Investigation of the composition of solar and interstellar matter using solar wind and pickup ion measurements with SWICS and SWIMS on the ACE spacecraft, *Space Sci. Rev*, *86*, 497.

Hefti, S., et al. (1998), Kinetic properties of solar wind minor ions and protons measured with SOHO/CELIAS, *J. Geophys. Res.*, *103*(A12), 29,697–29,704.

Hundhausen, A. J., H. Gilbert, and S. Bame (1968), Ionization state of the interplanetary plasma, *J. Geophys. Res.*, *73*(17), 5485–5493.

Ko, Y.-K., L. A. Fisk, G. Gloeckler, and J. Geiss (1996), Limitations on suprathermal tails of electrons in the lower solar corona, *Geophys. Res. Lett.*, *23*(20), 2785–2788.

Laming, J. M., and S. T. Lepri (2007), Ion charge states in the fast solar wind: New data analysis and theoretical refinements, *Astrophys. J.*, *660*, 1642.

Mazzotta, P., G. Mazzitelli, S. Colafrancesco, and N. Vittorio (1998), Ionization balance for optically thin plasmas: Rate coefficients for all atoms and ions of the elements H to Ni, *Astron. Astrophys. Suppl.*, *133*, 403.

McComas, D. J., R. W. Ebert, H. A. Elliott, B. E. Goldstein, J. T. Gosling, N. A. Schwadron, and R. M. Skoug (2008), Weaker solar wind from the polar coronal holes and the whole sun, *Geophys. Res. Lett.*, *35*, L18103, doi:10.1029/2008GL034896.

McFadden, et al. (2007), In-flight instrument calibration and performance verification, in *Calibration of Particle Instruments in Space Physics*, *ISSI Sci. Rep.*, vol. SR-007, edited by M. Wüest, D. S. Evans, and R. von Steiger, chap. 4, pp. 277–385, Eur. Space Agency, Noordwijk, Netherlands.

Owocki, S. P., and J. D. Scudder (1983), The effect of a non-Maxwellian electron distribution on oxygen and iron ionization balances in the solar corona, *Astrophys. J.*, *270*, 758–768.

Smith, E. J., and A. Balogh (2008), Decrease in heliospheric magnetic flux in this solar minimum: Recent Ulysses magnetic field observations, *Geophys. Res. Lett.*, *35*, L22103, doi:10.1029/2008GL035345.

Svalgaard, L., and E. W. Cliver (2007), A floor in the solar wind magnetic field, *Astrophys. J.*, *661*, L203, doi:10.1086/518786.

Timothy, J. G. (1981), Curved-channel microchannel array plates, *Rev. Sci. Instrum.*, *52*, 1131–1142, doi:10.1063/1.1136749.

von Steiger, R. (1995), Composition of the solar wind, habilitation thesis, University of Bern.

von Steiger, R. (1996), Solar wind composition and charge states, in *Solar Wind Eight*, edited by D. Winterhalter et al., *AIP Conf. Proc.*, 382, 193–198.

von Steiger, R. (2008), The solar wind throughout the solar cycle, in *The Heliosphere through the Solar Activity Cycle*, edited by A. Balogh, L. J. Lanzerotti, and S. T. Suess, chap. 3, pp. 41–78, Springer Praxis, Chichester, U. K.

von Steiger, R., and T. H. Zurbuchen (2006), Kinetic properties of heavy solar wind ions from ulysses-swics, *Geophys. Res. Lett.*, *33*, L09103, doi:10.1029/2005GL024998.

von Steiger, R., J. Geiss, and G. Gloeckler (1997), Composition of the solar wind, in *Cosmic Winds and the Heliosphere*, edited by J. R. Jokipii, C. P. Sonett, and M. S. Giampapa, pp. 581–616, Univ. of Ariz. Press, Tucson.

von Steiger, R., N. A. Schwadron, L. A. Fisk, J. Geiss, G. Gloeckler, S. Hefti, B. Wilken, R. F. Wimmer-Schweingruber, and T. H. Zurbuchen (2000), Composition of quasi-stationary solar wind flows from Ulysses/Solar Wind Ion Composition Spectrometer, *J. Geophys. Res.*, *105*(A12), 27,217–27,238.

von Steiger, R., T. H. Zurbuchen, and A. Kilchenmann (2004), Composition of interplanetary coronal mass ejections at very high latitudes, *Eos Trans. AGU*, *85*(47), Fall Meet. Suppl., Abstract SH33B-02.

Wilhelm, K., P. Lemaire, I. E. Dammasch, J. Hollandt, U. Schuehle, W. Curdt, T. Kucera, D. M. Hassler, and M. C. E. Huber (1998), Solar irradiances and radiances of uv and euv lines during the minimum of sunspot activity in 1996, *Astron. Astrophys.*, *334*, 685.

Zurbuchen, T. H. (2007), A new view of the coupling of the sun and the heliosphere, *Ann. Rev. Astron. Astrophys.*, *45*, 297.

Zurbuchen, T. H., and I. G. Richardson (2006), In-situ solar wind and magnetic field signatures of interplanetary coronal mass ejections, *Space Sci. Rev.*, *123*, 31–43.

R. von Steiger, International Space Science Institute, Hallerstrasse 6, CH-3012 Bern, Switzerland. (vsteiger@issibern.ch)

T. H. Zurbuchen, Department of Atmospheric, Oceanic and Space Sciences, University of Michigan, 2455 Hayward St., Ann Arbor, MI 48109, USA. (thomasz@umich.edu)